Disproportionation of Iron in Almandine-Pyrope-Grossular Garnet From 25 to 65 GPa

K. E. Swadba[1] , A. H. Davis[2] , C. C. Zurkowski[3], S. Chariton[4], V. B. Prakapenka[4] , and A. J. Campbell[1]

[1]Department of the Geophysical Sciences, University of Chicago, Chicago, IL, USA, [2]Centre for Earth Evolution and Dynamics (CEED), University of Oslo, Oslo, Norway, [3]Lawrence Livermore National Laboratory, Livermore, CA, USA, [4]Center for Advanced Radiation Sources, University of Chicago, Chicago, IL, USA

Abstract The production of metal via the iron disproportionation reaction in the deep Earth has been a long debated topic with important implications for the geochemistry of the lower mantle. To explore the occurrence of the iron disproportionation reaction from 25 to 65 GPa, a natural almandine-pyrope-grossular garnet was studied with in situ X-ray diffraction (XRD) in the laser-heated diamond anvil cell and ex situ scanning electron microscopy (SEM) techniques. Upon heating the natural almandine-pyrope-grossular garnet up to 3000 K up to 65 GPa, the formation of phase assemblage consisting of bridgmanite, stishovite, and davemaoite was confirmed by XRD, but because of the low abundance of Fe metal and small grain size, XRD was determined not to be effective in detecting the disproportionation reaction. Examination of the samples recovered between 39 and 64 GPa by SEM analysis revealed the presence of nm-scale disproportionated iron metal grains as an additional product of this reaction that was not detectable in the XRD patterns. Volume compression data of bridgmanite synthesized in the experiments were fit to the Birch-Murnaghan equation of state and compared to similar compositions. Bridgmanite was found to decompress to the LiNbO$_3$-type structure, indicating a high FeAlO$_3$ content, in accordance with the occurrence of a disproportionation reaction. The experimental confirmation of disproportionated metallic Fe has significant implications for the distribution of siderophile and volatile elements in the lower mantle.

Plain Language Summary An Fe- and Al-rich garnet was studied with X-ray diffraction (XRD) in a laser-heated diamond anvil cell and scanning electron microscopy (SEM) techniques to explore the behavior of Fe in mineral assemblages at conditions relevant to Earth's lower mantle. We experimentally investigate the iron disproportionation reaction, during which Fe^{2+} is both oxidized into Fe^{3+} and reduced into Fe^0. This study confirms the formation of a mineral phase assemblage consisting of bridgmanite, stishovite, and davemaoite through XRD, but because of the low abundance of Fe metal and small grain size, XRD was not sufficient to detect the disproportionation reaction. Examination of the recovered product by SEM revealed disproportionated iron metal in several samples. Volume compression data were also collected, and, notably, bridgmanite was found to decompress to a different structure at ambient pressure, indicating a high FeAlO$_3$ content, in accordance with the occurrence of a disproportionation reaction. The experimental confirmation of disproportionated metallic Fe has significant implications for the siderophile element geochemistry of the lower mantle.

1. Introduction

It is well established that bridgmanite is likely the most abundant mineral in the lower mantle and adopts the perovskite *Pbnm* structure (Knittle & Jeanloz, 1987; L. G. Liu, 1976; O'Neill & Jeanloz, 1990). Bridgmanite ((Mg,Fe) (Si,Al)O$_3$) can accommodate several different cation substitutions into its perovskite structure (ABO$_3$). Specifically, it has been extensively shown that the trivalent cations Fe^{3+} and Al^{3+} can be incorporated through a charge-coupled substitution, with Al^{3+} entering the B site and stabilizing Fe^{3+} in the A site (Frost & Langenhorst, 2002; Lauterbach et al., 2000; Z. Liu et al., 2020; McCammon, 1997; Richmond & Brodholt, 1998; Vanpeteghem et al., 2006). Because Al has a chemical preference for the bridgmanite structure, when Al is present along with Fe in the phase assemblage, the disproportionation reaction will be promoted. In an Fe^{2+}-rich starting composition, the incorporation of an FeAlO$_3$ component into bridgmanite can occur through the disproportionation of Fe according to the following reaction: 3Fe^{2+} → 2Fe^{3+}+Fe^0. Although this reaction produces a small volume of metallic iron, it has been suggested that this disproportionation reaction plays a critical role in

the geochemistry of the lower mantle (Frost et al., 2004). Studies have also suggested that the disproportionation reaction may proceed to different degrees as a function of depth (Shim et al., 2017; Tsujino et al., 2023). The occurrence of this reaction and the creation of small amounts of metallic Fe can have significant implications for the siderophile element geochemistry of the lower mantle, notably through its impact on isotopic tracers such as Re and Os and on platinum group element distributions. Metallic Fe could also serve as a likely host for volatile elements in the lower mantle, such as C, S, and H, which are known to easily alloy with iron at relevant pressures and temperatures. The presence of metallic iron in the lower mantle presents a reservoir to store these elements and would notably impact the distribution of volatile elements in the Earth's deep interior.

It has been shown that garnets along the pyrope-almandine join form bridgmanite assemblages at high pressure and temperature conditions (Dorfman et al., 2012; Irifune et al., 1996; Kesson et al., 1995). Because pyrope-almandine garnets have both ferrous Fe and Al, the Fe disproportionation reaction is likely to occur during the formation of bridgmanite, resulting in the incorporation of the $FeAlO_3$ component in bridgmanite and the production of accompanying metallic Fe. However, there has been no consistent identification of Fe disproportionation occurring in pyrope-almandine garnet samples in existing experimental studies. Kesson et al. (1995) performed transmission electron microscopy (TEM) analyses on garnet samples recovered from high pressure and temperature in the diamond anvil cell (DAC) and noted the existence of "blebs and runnels of an Fe-rich phase" at grain boundaries, accompanied by minor amounts of stishovite, but they did not identify disproportionated metallic Fe. Similarly, Dorfman et al. (2012) found no evidence of Fe disproportionation in garnet samples analyzed with synchrotron X-ray diffraction (XRD).

In this work, we investigate the disproportionation of Fe in a natural almandine-pyrope-grossular garnet to 65 GPa and 3500 K with in situ XRD in the laser-heated DAC and ex situ scanning electron microscopy (SEM) analysis on recovered samples. The results will inform our understanding of Fe disproportionation reactions in the Earth's mantle.

2. Materials and Methods

A natural almandine-pyrope-grossular garnet was selected for this study. The composition was determined by wavelength-dispersive X-ray spectroscopy (WDS) at the University of Maryland to be $Alm_{52}Pyr_{34}Grs_{11}Sps_2And_1$. Measurements are given in Table S1 in Supporting Information S1. The $Fe^{3+}/\Sigma Fe$ ratio of the starting material was determined to be 0.016 based on the stoichiometry of the WDS analyses. This garnet was selected for its high Fe^{2+} and Al content, which should increase the amount of Fe disproportionation that will occur. For all experiments, the natural garnet was broken into small fragments, which were loaded either with an Ir foil to act as an internal pressure calibrant and laser absorber, or with no foil. Samples were loaded in 50–100 μm-sized holes drilled through pre-indented Re or Ni gaskets. Symmetric diamond anvil cells with 250–300 μm culets were used to achieve pressures up to 65 GPa. Pressures were determined using the Ir equation of state (Cerenius & Dubrovinsky, 2000) or Raman spectroscopy on the diamond anvil culets before and after laser-heating (Akahama & Kawamura, 2004). Pressures at high temperatures were calculated with the approximation of a 1% increase in pre-heat pressure per 250 K increase, after Fischer et al. (2015) and Chidester et al. (2017). Table 1 gives a list of experimental conditions and analysis details.

XRD was performed at the GSECARS beamline 13-ID-D (APS, Argonne National Laboratory). Diffraction patterns were collected using a CdTe 1M Pilatus detector. The position and orientation of the detector was calibrated using a LaB_6 NIST standard. The X-ray energy was tuned to either 37 keV (0.3344 Å) or 42 keV (0.2952 Å) and focused to full width, half max dimensions of 2×3 μm. Double-sided laser-heating of the samples was carried out with in situ XRD measurements (Prakapenka et al., 2008). 1,064 nm fiber lasers were shaped to ~10 μm radius flat tops and aligned with the X-ray beam. Temperatures were measured on both sides using spectroradiometry and fitting to a gray body approximation (Heinz & Jeanloz, 1987). Diffraction images were integrated to produce 1-D diffraction patterns using the Dioptas software (Prescher & Prakapenka, 2015).

One sample (K11) was heated with a 1,064 nm fiber laser at the University of Chicago. In this experiment, the laser spot size was approximately 15 μm and temperatures were measured on both sides by multispectral imaging radiometry (Campbell, 2008). XRD was performed at GSECARS on a recovered thin section from this sample.

The transition to bridgmanite in Fe-rich silicates is accompanied by a color change from transparent to dark brown (Kesson et al., 1995; O'Neill & Jeanloz, 1994). In most samples, the transformation from garnet to a

Table 1
Sample Details

Sample	Foil	Pre-heat pressure (GPa)	Post-heat pressure (GPa)	Estimated pressure at high temperature (GPa)	Temperature history	Heating time (min)	Analysis method	High P,T phases detected
K7_1	Ir	25	21	26.8	Flash then held ~2100 K	14	XRD	Sti
K8	Ir	28	27	30.3	Max 2380 K	5	XRD	Bdm, Sti
		–	5	–	Decompressed sample K8	–	XRD	Bdm, Sti
K7_2	Ir	39	35	43.7	Flash to 3000 K then held ~2000 K	20	XRD	Bdm, Sti, Dvm
K44_2	None	39	37	41.8	Heated on pre-heated (melted) spot; held ~2100 K	30	XRD + SEM	Bdm, Sti, Dvm, Fe^0
K44_1	None	47	39	52.1	Unknown max T; melted	15	XRD + SEM	Bdm, Sti, Dvm, Fe^0
K52_1	None	48	44	51.8	Flash to 2280 K then held ~2100 K	20	XRD	Bdm, Sti, Dvm
K47	None	51	51	54.5	Flash to unknown T then held ~2000 K	4	XRD	Bdm, Sti, Dvm
K11	None	52	No record	57.6	Melted and slowly cooled	4	XRD + SEM	Bdm, Sti, Dm, Crn, Fe^0
K52_2	None	54	55	60.0	Flash to 3100 K then held ~2300 K	30	XRD	Bdm, Sti, Dvm
K7_3	Ir	53	55	58.7	No flash; gradual increase to ~3000 K	8	XRD	Bdm
K54	None	64	59	68.9	No flash; held ~2200 K	30	XRD + SEM	Bdm, Sti, Dvm, Crn, Fe^0

Note. Pressure was recorded either form Ir foil or Diamond Raman spectroscopy. Bdm = bridgmanite, Sti = stishovite, Dvm = davemaoite, Crn = corundum, and Fe^0 = metallic Fe. Sample K8 was decompressed to 5 GPa and measured at 300 K with no laser heating.

bridgmanite assemblage was accompanied by a sudden increase in laser coupling, observed as a flash accompanied by a sudden spike in temperature. Similar heating experiences are detailed in Dorfman et al. (2012). Laser power was adjusted during these intervals to attempt to maintain stable temperatures. All samples were quenched from high temperatures with the exception of K11, which was slowly cooled.

Several samples were recovered from high pressure and temperature conditions and prepared for SEM analysis using the focused ion beam (FIB) in the Tescan Lyra3 field-emission SEM in the Department of the Geophysical Sciences at the University of Chicago. A 30 kV Ga^+ beam operating at 1–5 nA was used to mill a section from the center of the laser-heated spot, and sections measuring approximately $15 \times 10 \times 2$ µm were lifted out and attached to a copper TEM grid. Sections were further thinned to ~1 µm using lower operating currents (50–500 pA). Backscattered electron (BSE) images were collected at an acceleration voltage of 5–10 kV. Chemical analyses were performed with the same range of acceleration voltages using energy dispersive X-ray spectroscopy (EDS) on the same Tescan instrument, and compositions were obtained using Oxford Instruments Aztec software. The spatial resolution of the measurements was ~1 µm.

3. Results

3.1. XRD Results

The synchrotron XRD experiments were used to establish which phases are detectable at high pressures and temperatures in almandine-pyrope-grossular garnet using in situ techniques. The sample pressure ranged from 5 to 55 GPa in these experiments. To allow for comparison of high pressure and ambient pressure diffraction patterns, sample K8 was compressed to 28 GPa, heated for 10 min up to 2300 K, quenched, and then decompressed to 5 GPa (Figure 1). The high pressure and temperature diffraction pattern shows bridgmanite and stishovite in addition to untransformed garnet, and the decompressed pattern shows the same phases. Neither pattern had evidence for fcc, hcp, or bcc iron. Garnet persists in these patterns because the X-ray beam passes through a thin layer of unheated sample material adjacent to the diamonds. Dorfman et al. (2012) also notes that peaks corresponding to untransformed garnet persist in several samples at high pressures even after heating at 2000 K for 30 or more minutes. They attribute this to the sluggish transformation from metastable crystalline garnet to perovskite. In this pattern and all other patterns, stishovite can be
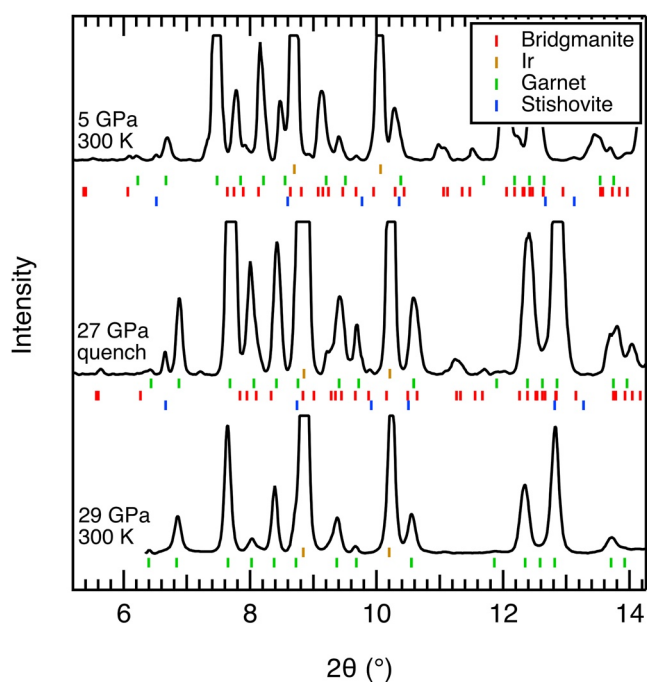
Figure 1. X-ray diffraction patterns collected at 37 keV on a sample with an Ir foil (K8). From bottom to top, patterns correspond to unheated garnet at 29 GPa, the quench pattern, and a decompressed 5 GPa pattern. The tops of the most intense peaks have been truncated.
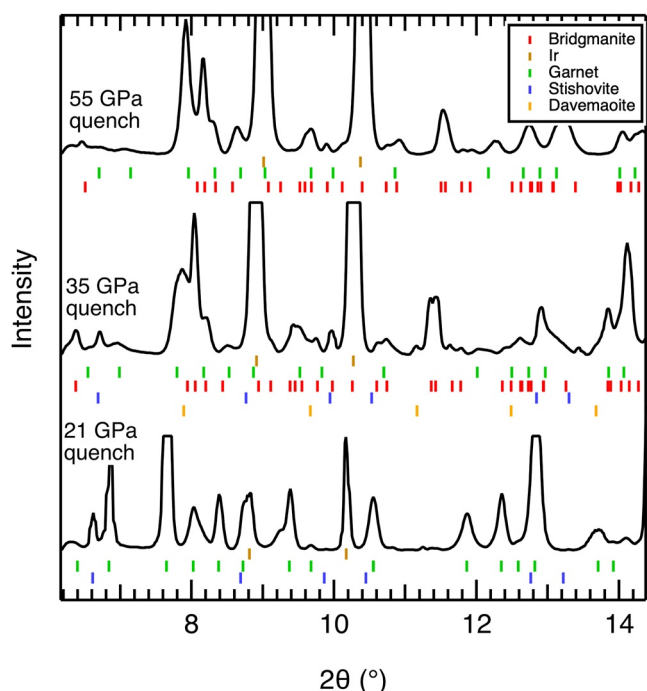

Figure 2. X-ray diffraction patterns collected at 37 keV on a sample with an Ir foil (K7_1, K7_2, and K7_3). Quench patterns at 21, 35, and 55 GPa.

identified through the strong 110 peak. Generally, the 020, 112, and 200 triplet is diagnostic for the bridgmanite phase, and the low-angle 002, 110, and 111 peaks can be used to identify bridgmanite if there is a high level of peak overlap at higher angles.

To further explore the detectable phase assemblage at higher pressures, another sample loaded with Ir foil was heated at three different pressures (K7_1, K7_2, and K7_3) (Figure 2). At 21 GPa, the pattern quenched from 2100 K contains only stishovite and untransformed garnet. At 35 GPa, the pattern quenched from 2000 K contains stishovite, bridgmanite, davemao-ite, and untransformed garnet. The pattern quenched from 3000 K at 55 GPa contains bridgmanite and untransformed garnet. Several additional samples were prepared without Ir foil and heated with in situ XRD monitoring to assess any differences in heating progression and resultant phases if Ir is not present. Quenched XRD patterns for samples with no Ir foil were collected at 42 keV and are shown in Figure S1 in Supporting Information S1. These patterns, ranging from quench pressures of 37–59 GPa, show evidence of stishovite, bridgmanite, davemaoite, and untransformed garnet. The dave-maoite is identified primarily through the 200 and 211 peaks, and the lattice parameters appear to be slightly larger than would be expected for pure $CaSiO_3$. Shim et al. (2000) note that the 200 lines of $CaSiO_3$ perovskite yield larger unit cell parameters than other lines as a result of non-hydrostatic stresses in the sample. The composition of the davemaoite will be discussed further below. Corundum or ilmenite structured $(Al,Fe)_2O_3$ cannot be uniquely identified in each pattern because of the peak overlap, but it may exist in the heated samples. Ferropericlase similarly cannot be uniquely identified in each pattern because of the peak overlap but may exist in the heated samples. Synchrotron XRD measurements were also performed on a thin section of sample K11, which was recovered and thinned using the FIB to a thickness of 1 μm. While the patterns are dominated by the Cu grid and Pt coating deposited during the FIB recovery process, we can also identify untransformed garnet, stishovite, the $LiNbO_3$-type structure, and FeO (Figure S2 in Supporting Information S1).

3.2. SEM Results

SEM analyses were conducted on several recovered samples to determine what phases could be detected using ex situ techniques (Table 1); two examples are presented here. Sample K11 was compressed to 52 GPa, melted (maximum temperature ~3300 K), and cooled slowly to allow the growth of large observable crystals. The BSE image of the recovered section clearly reveals textures related to the temperature gradient that was generated during the heating and cooling of the sample (Figure 3). One can identify the boundary separating the untransformed starting material from the rest of the sample (red dashed line in Figure 3). Outside this boundary, temperatures were not high enough to promote any transformation of the garnet, while immediately inside the boundary, temperatures were high enough to promote sub-solidus phase transitions but not high enough for melting to occur. Grains in this region reach a maximum of ~100 nm in size. Further inward, textural changes reveal the solidus (orange dashed line in Figure 3) beyond which melt coexisted with solid phases. The outermost portion of this region is dominated by micron-sized Al-rich grains, followed by micron-sized grains of stishovite embedded in a bridgmanite matrix. The matrix is scattered with 100 nm-sized grains of metallic Fe, indicating that the disproportionation reaction did occur. We provide details below on how a metallic Fe grain is
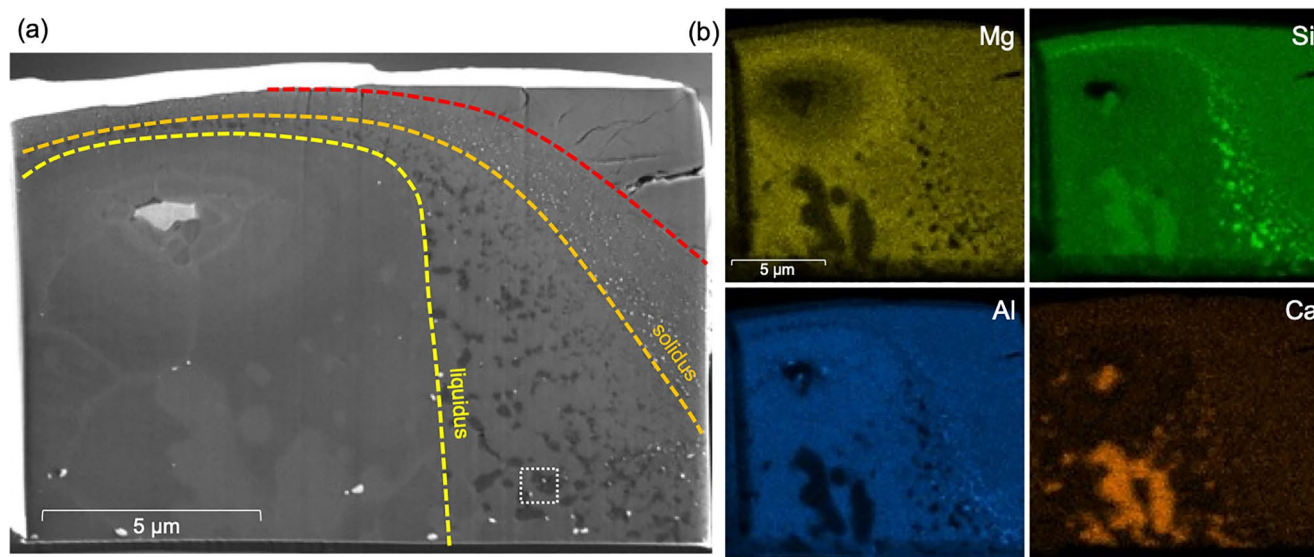
Figure 3. (a) Backscattered electron image collected at 5 kV of a section recovered from 52 GPa that was melted (3300 K) and slowly cooled (K11). Red, orange, and yellow lines indicate the edge of the laser-heated spot, solidus, and liquidus, respectively. The dashed box indicates the region of interest mapped in Figure 4. (b) EDS maps collected at 7 kV (Si, Al, and Mg) and 10 kV (Ca).

identified. The 100-nm sized grains are identified as metallic Fe based upon the standard BSE albedo that we find for the metallic Fe grains. It is improbable that the Fe metal was produced through only reduction because we find Fe in the silicate and only see a small amount of Fe metal on the scale expected for disproportionation rather than a reduction from an external reactant. Inward from the solidus, we identify the liquidus, beyond which the sample texture is characterized by the gradual cooling history of the liquidus melt composition. Several large grains of davemaoite grew from the melt along with small grains of metallic Fe. As cooling progressed, the melt became enriched in Fe and depleted in Mg, as seen in the EDS maps.

Table 2 shows averages of EDS measurements collected at 5 kV on the largest selected grains in K11. Because of small grain sizes and potential beam overlap, these measurements may not represent the true composition of the phases present. A composition for bridgmanite is not provided as these grains were too small to measure. The subsolidus region should contain the same phases present in larger sizes between the solidus and liquidus: bridgmanite, metallic Fe, davemaoite, stishovite, and Al-rich phase. An EDS map of a region between the solidus and liquidus shows grains smaller than 250 nm in diameter (Figure 4). The Mg and Fe maps reveal the background bridgmanite matrix, while the Si map highlights the stishovite grains, and the Al map highlights the Al-rich grains. Hotspots in the Fe map reveal the metallic iron grains. The Ca map reveals an even distribution

Table 2
Average Elemental Quantities in Atomic % for Different Phases and Regions Collected at 5 kV on Sample K11

Phase	O	Mg	Al	Si	Ca	Fe
Stishovite ($n = 3$)	61.9 (0.5)	2.67 (0.05)	4.54 (0.08)	24.9 (0.1)	1.5 (0.6)	4.5 (0.2)
Davemaoite ($n = 4$)	59.0 (0.3)	1.63 (0.15)	2.00 (0.14)	18.5 (0.4)	15.0 (0.6)	3.91 (0.16)
Garnet ($n = 1$)	57.32	5.17	9.94	14.38	2.57	10.62
Center ($n = 3$)	48.6 (0.4)	0.75 (0.06)	1.53 (0.02)	0.4 (0.3)	0.05 (0.09)	48.7 (0.8)
Subsolidus ($n = 8$)	57.2 (1.0)	5.2 (0.3)	10.2 (0.3)	14.8 (0.5)	2.0 (0.4)	10.6 (1.4)
Fe grain ($n = 1$)	48.45	5.25	9.88	10.45	0.68	25.28

Note. The number of point analyses used for measurement is given by *n* in parentheses. Standard deviations are given in parentheses below atomic % values. Instrumental uncertainty is typically 5% relative accuracy (Chidester et al., 2017). Measurements on small grains include overlap with adjacent grains. Center refers to the brightest region (melt) at the center of the laser-heated spot. Subsolidus refers to measurements taken over the subsolidus region between the orange and red lines in Figure 3.
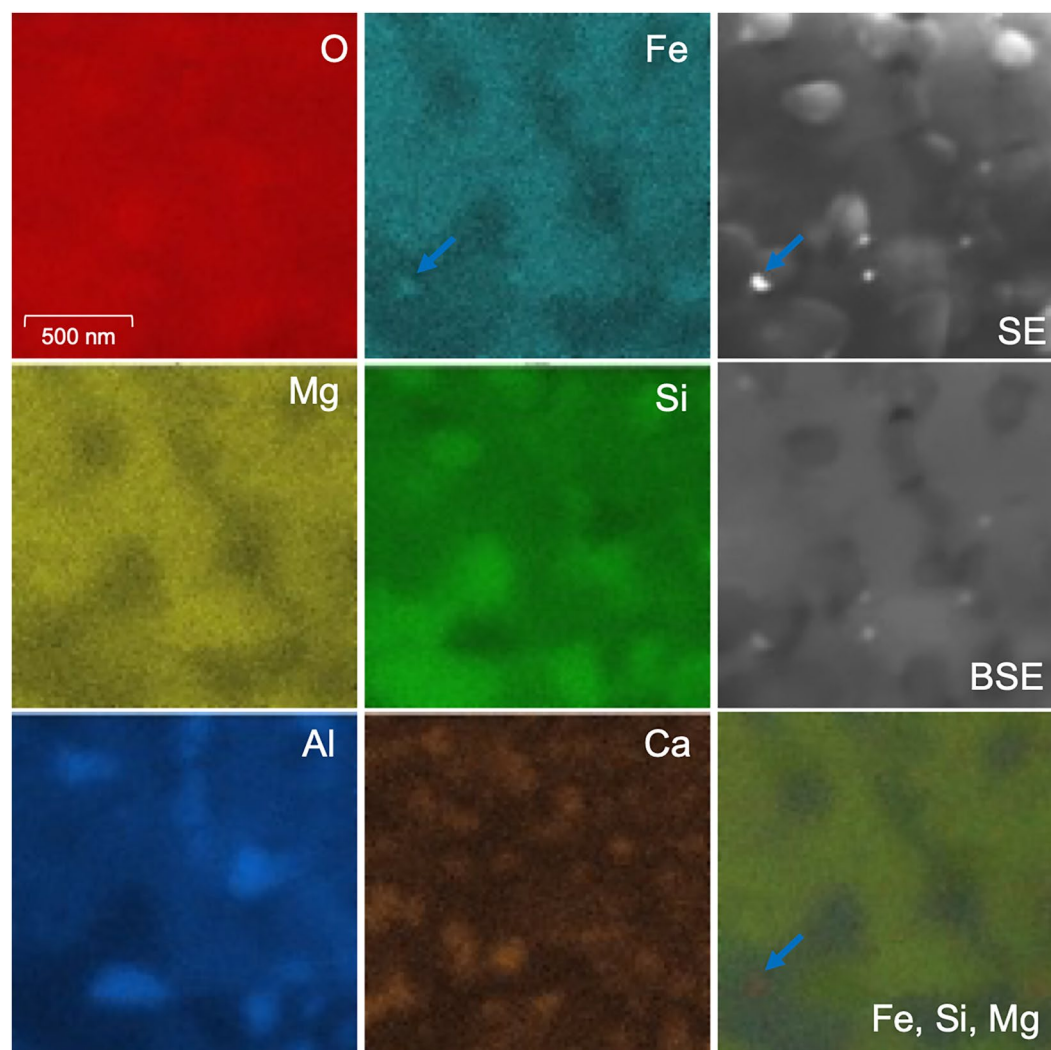
Figure 4. EDS maps collected on sample K11 at 5 kV as well as SE and Backscattered electron images of the region of interest (shown on larger image in Figure 3a). A layered map including the Fe, Si, and Mg measurements is shown in the bottom right (Fe = red, Si = blue, and Mg = green). Blue arrows indicate the largest metallic iron grains in the region.

of davemaoite. Because the disproportionated metallic Fe grains are so small, EDS spectra pick up signals from the grain as well as the surrounding material. Point measurements taken in a line across such grains, however, show a spike in Fe content at the expense of all other elements, including O, indicating that these grains are likely metallic Fe (Figure 5). Disproportionation is evident in both the subsolidus and partially melted regions of this garnet at 52 GPa, as revealed in this recovered section with BSE imaging.

To establish the occurrence of Fe disproportionation at higher pressure, we also performed recovery, imaging, and EDS mapping on sample K54, which was compressed to 64 GPa, heated at ~2200 K for 30 min with in situ XRD collection, and quenched. Both the SE and BSE images of the recovered section reveal the new assemblage created within the laser-heated spot and the untransformed garnet outside the hot region (Figure 6). Similar to the previous thin section, there is a subsolidus region adjacent to the untransformed garnet defined by nm-sized grains. Further inwards toward the center of the spot, we can observe a ring of Al enrichment and a ring of Si enrichment, similar to what was seen in the previous sample. EDS maps of the laser-heated region (Figure S3 in Supporting Information S1) and point analyses along a line through the laser-heated spot (Figure S4 in Supporting Information S1) show that the center of the heated region is depleted in Si and slightly enriched in Al. EDS spectra reconstructed from the EDS maps show that the region with a mixture of bright and dark grains has the same bulk composition as the garnet starting material. The bright grains in this ring are identified as disproportionated
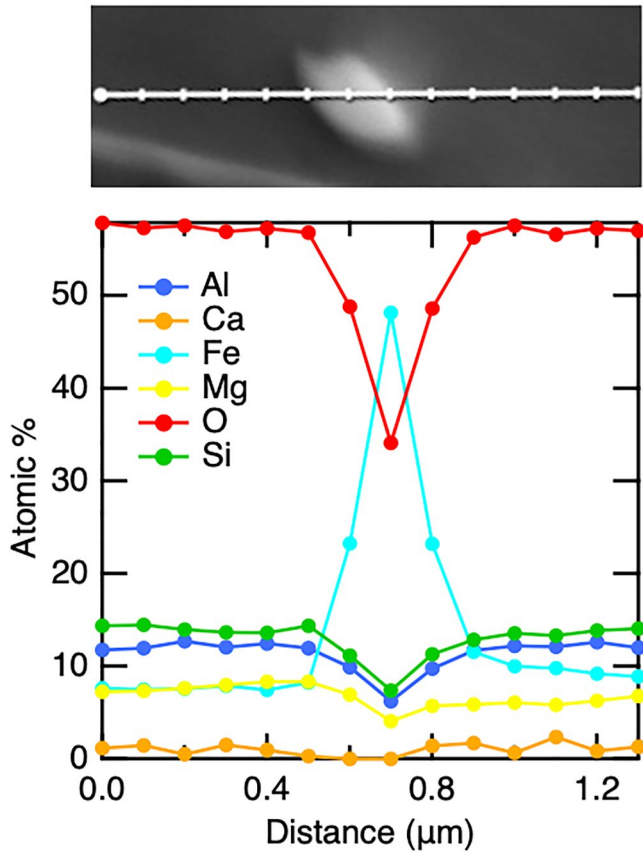
Figure 5. Line scan across a metallic iron grain in sample K11 collected at 5 kV.

metallic Fe, similar to those seen in the previous section, while the dark grains are identified as stishovite. Overall, textures seen in the 64 GPa section (Figure 6) are similar to those seen in the 52 GPa section (Figure 3).

4. Discussion

No metallic Fe was detectable in any of the XRD patterns from 5 to 64 GPa, but metallic Fe was clearly found in each of the recovered sections between 39 and 64 GPa. These findings demonstrate the possibility for Fe disproportionation to go undetected in samples that are probed only with XRD techniques. The size of the disproportionated Fe grains as well as the presence of accompanying bridgmanite with its myriad and overlapping peaks prevent the metallic Fe phase from being identified in XRD patterns. The presence of metallic Fe in the recovered sections, however, demonstrates that the Fe disproportionation reaction has occurred, indicating that Fe^{3+} was created alongside the metallic Fe according to the following reaction:

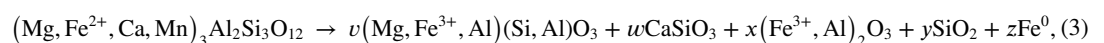$$Fe_3^{2+}Al_2Si_3O_{12} \rightarrow 2Fe^{3+}AlO_3 + 3SiO_2 + Fe^0. \tag{1}$$
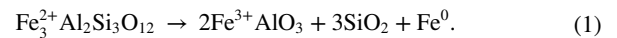
This reaction is simplified here to the decomposition of pure endmember almandine only, neglecting the pyrope, grossular, and spessartine components of the studied composition. In this reaction, Fe^{3+} enters the A site of the bridgmanite phase, shown as an $FeAlO_3$ component. Stishovite is also created along with metallic Fe. While the XRD results confirm the creation of only bridgmanite and stishovite, the SEM results reveal all three phases present in reaction 1. At lower pressure and temperature conditions where bridgmanite is not stable, almandine will decompose according to the following reaction:

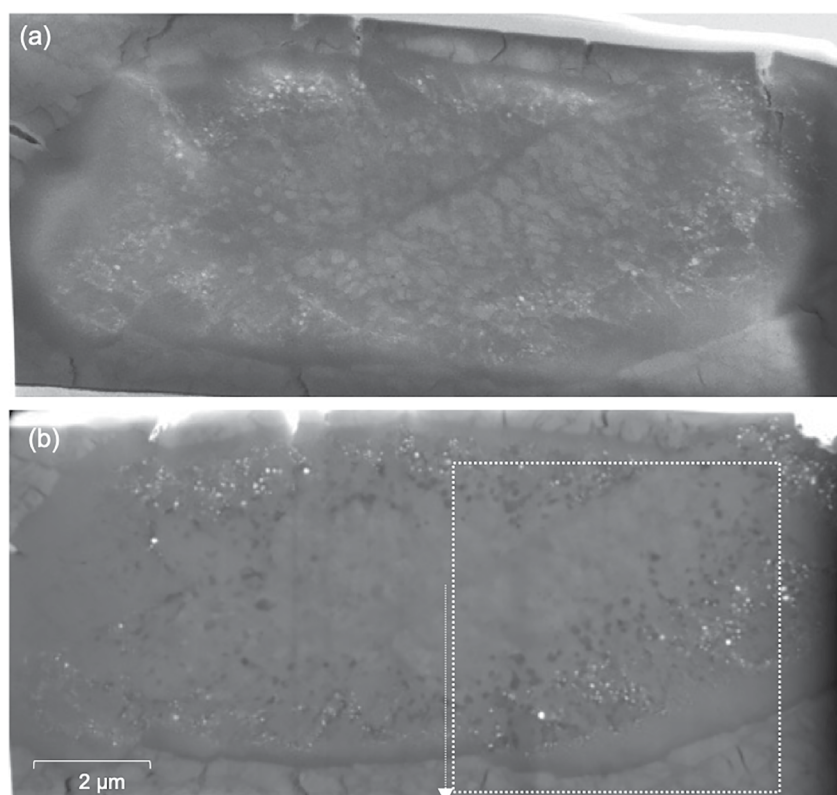$$Fe_3^{2+}Al_2Si_3O_{12} \rightarrow Al_2O_3 + 3SiO_2 + 3Fe^{2+}O. \tag{2}$$
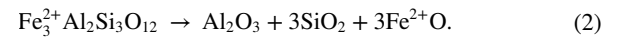
This decomposition reaction has been observed in experiments on pure almandine (Akaogi et al., 1998; Conrad et al., 1996; Dorfman et al., 2012). The results of reaction 2 can be seen in K7_1, which had a starting pressure of 25 GPa and showed only stishovite without bridgmanite in the XRD pattern (Figure 2). The untransformed garnet and Ir peaks likely obscured the wüstite and corundum peaks in this pattern. This sample was not recovered and imaged with the SEM, so we do not have conclusive proof of the existence or absence of metallic Fe, but the absence of bridgmanite suggests that reaction 1 did not occur at 25 GPa in this garnet composition.
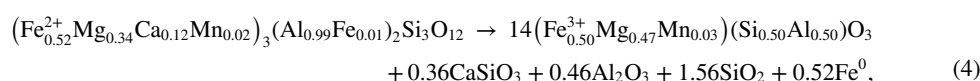
While our XRD results can confirm the presence of stishovite and bridgmanite in accordance with Equation 1, we note that corundum (or an ilmenite-structured Al-rich phase) cannot be ruled out as a phase present in the patterns as the peaks could be obscured by the other phases present, and we do detect Al-rich grains in the recovered thin sections in areas of partial melt (see Figures 3 and 4, Figure S3 in Supporting Information S1). Z. Liu et al. (2017) demonstrated that for a pyrope composition, bridgmanite and corundum can coexist at 42 GPa and 2000 K, with Al entering the bridgmanite phase and Mg entering the corundum phase. When Fe is present, we can also expect Fe^{3+} to be incorporated into the corundum phase. The incorporation of Fe^{3+} into the Al phase in addition to its incorporation into bridgmanite further serves to drive the disproportionation reaction. Additionally, we note that ferropericlase ((Mg,Fe)O) cannot be ruled out as a phase present in the patterns in addition to the metallic Fe. Both reactions 1 and 2 could thus take place at the same time to produce both FeO and Fe metal as reaction products. Because we do not find conclusive evidence for the existence of FeO in the SEM results, in the following discussion, we will neglect the potential production of FeO. Finally, the coexistence of davemaoite with the above phases is expected from the grossular and andradite components of our starting material. An Al- and Fe-rich phase can be created in conjunction with bridgmanite, davemaoite, stishovite, and metallic Fe through the following general reaction:

$$(Mg, Fe^{2+}, Ca, Mn)_3Al_2Si_3O_{12} \rightarrow \upsilon(Mg, Fe^{3+}, Al)(Si, Al)O_3 + wCaSiO_3 + x(Fe^{3+}, Al)_2O_3 + ySiO_2 + zFe^0, \tag{3}$$

Figure 6. (a) SE and (b) Backscattered electron (BSE) images of a section recovered from 64 GPa that was heated at ~2200 K for 30 min (K54). The small white dots in the BSE image are metallic iron and are abundant around the edges of the laser-heated spot. The white dotted box and the arrow show the map region and line scan of Figures S3 and S4 in Supporting Information S1, respectively.

where v, w, x, y, and z represent coefficients that vary according to how the components partition between phases. The reaction corresponding to the composition in this study ($Alm_{52}Pyr_{34}Grs_{11}Sps_2And_1$) is as follows:

$$\left(Fe^{2+}_{0.52}Mg_{0.34}Ca_{0.12}Mn_{0.02}\right)_3\left(Al_{0.99}Fe_{0.01}\right)_2Si_3O_{12} \rightarrow 14\left(Fe^{3+}_{0.50}Mg_{0.47}Mn_{0.03}\right)\left(Si_{0.50}Al_{0.50}\right)O_3$$
$$+ 0.36CaSiO_3 + 0.46Al_2O_3 + 1.56SiO_2 + 0.52Fe^0, \tag{4}$$

with the following assumptions: all Fe^{2+} is disproportionated, all $FeAlO_3$ component enters bridgmanite (not corundum), all Al_2O_3 component enters corundum (not bridgmanite), and davemaoite is endmember $CaSiO_3$. In the samples in this study, the occurrence of a ring of stishovite grains closer to the center of the laser-heated spot surrounded by a ring of Al-rich grains can be explained by the existence of a temperature gradient in this partial melt region. While the temperature gradient indicates nonequilibrium across the entire laser-heated spot, we assume local equilibrium at each point along the temperature gradient. This will be further explored in the discussion section below.

The PerpleX thermodynamic calculation package (Connolly, 2005) can be used with the thermodynamic database provided by Stixrude and Lithgow-Bertelloni (2022) to predict the phase assemblage at our experimental conditions for our specific composition, and the results match well with our observations from the XRD and SEM results. Details are given in Supporting Information S1 regarding the modification of the PerpleX input files to allow for the Fe disproportionation reaction to occur (Table S2 in Supporting Information S1). Figure 7a shows the PerpleX phase assemblage predictions in 2100, 2300, and 2500 K from 20 to 80 GPa. In the lower mantle pressure region, we predict the occurrence of garnet, bridgmanite, stishovite, davemaoite, corundum, and fcc/hcp Fe, and the presence of each of these phases is confirmed in our XRD and SEM results. Based on the PerpleX prediction, one expects to see ~3 mol% metallic Fe, which aligns with our SEM images (Figures 3 and 6). Because the starting material has such high Fe^{2+} and Al contents, the amount of disproportionated metallic Fe is larger than that expected from a pyrolitic composition representing the lower mantle, which has been predicted to be ~1 wt% (Frost et al., 2004). With increasing temperature, Al_2O_3 increasingly enters bridgmanite, resulting in
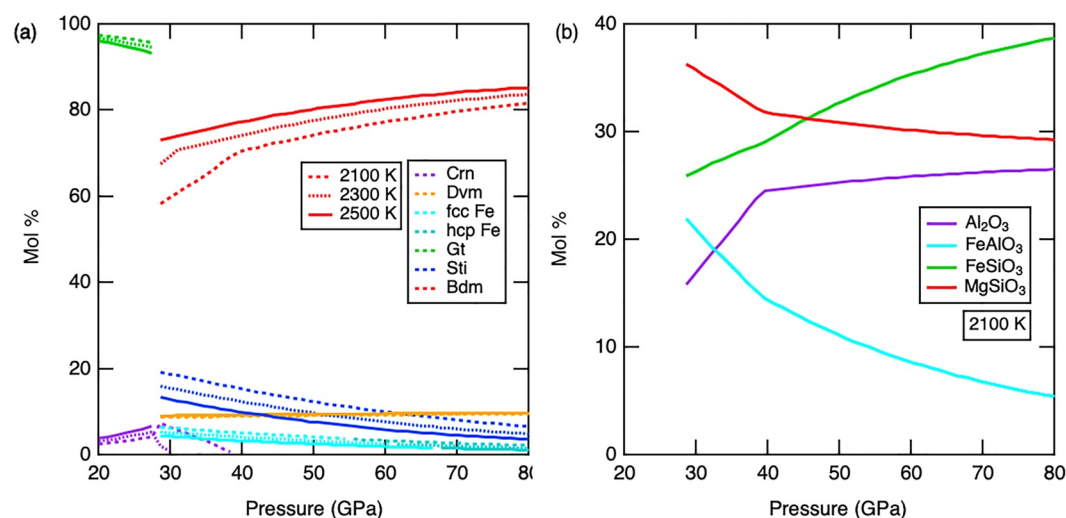
Figure 7. PerpleX predictions for our garnet composition. (a) Phase assemblage prediction at 2100, 2300, and 2500 K. (b) Prediction of bridgmanite composition by endmember components for 2100 K.

the disappearance of corundum at lower pressures as temperature increases. The occurrence of corundum in rings in our SEM samples can thus be confirmed as a consequence of the temperature gradient within the laser-heated spot as suggested above. The amount of stishovite present decreases with increasing temperature but does not vanish.

Our XRD results confirming the transformation of majority almandine-pyrope-grossular garnet into bridgmanite and stishovite are also in alignment with previous work. Dorfman et al. (2012) noted that for their Alm38 composition, heating at 38 GPa produced a mixture of bridgmanite and oxides, and with increasing pressure, the ratio of bridgmanite to oxides increased, leading bridgmanite to be the dominant phase by 45 GPa. Additionally, all compositions showed stishovite diffraction peaks on decompression and heating between 59 and 71 GPa. It is possible that the presence of stishovite indicates that disproportionation occurred following reaction 1. However, in an Alm54 sample compressed to 74 GPa and then decompressed to 23 GPa and re-heated for 10 min at 1100 K, they observed a reversion to only the garnet phase, which they take to indicate that a high-pressure single phase bridgmanite existed with no major compositional gradients. They also suggest that the recovery of garnet with no other detectable phases suggests that the synthesis of bridgmanite was not accompanied by significant oxidation of Fe^{2+} to ferric iron because this would have made it more difficult to re-synthesize a single phase garnet composition. Our SEM results on a sample recovered from 64 GPa show multiphase assemblage inside the laser-heated spot rather than a single bridgmanite phase with the same composition as the starting material. It can be observed, however, that in the subsolidus rim at the edge of the spot, bright metallic Fe grains are visible closest to the partial melt region and must also exist throughout the subsolidus rim in sizes too small to be seen. The PerpleX results for our composition also likewise suggest that bridgmanite will not exist as a single phase at high pressures and temperatures for our composition.

In the experiments of Kesson et al. (1995) on Alm50-Py50, Si-poor, Al-rich bridgmanite was found to coexist with stishovite at 50 GPa, and the same assemblage was observed at 60 GPa in addition to Fe in "hot spots." In the present study, all of the samples except one exhibited the bridgmanite phase coexisting with stishovite, which is consistent with the observations of Dorfman et al. (2012) and Kesson et al. (1995), even though the composition in this study is more complex than the almandine-pyrope-grossular compositions studied by either; specifically the garnet in this study contains Ca and small amounts of Mn (Table S1 in Supporting Information S1). The presence of Ca stabilizes davemaoite, as seen in the XRD and SEM results as well as the PerpleX results, which may influence the composition and stability of bridgmanite. It has been shown that from 40 to 110 GPa above 2300 K, davemaoite will dissolve into bridgmanite in a pyrolitic composition, but we observe davemaoite in all but one of our samples above 39 GPa, regardless of temperature, likely due to the high Ca content of our starting material (Ko et al., 2022). The composition of the davemaoite in this study, as given in Table 2, indicates that there are minor amounts of Mg, Fe, and Al in the phase. Studies have shown a solubility of Mg in davemaoite

between 5 and 10 mol% at 55 GPa and 2000 K (Armstrong et al., 2012). Fujino et al. (2004) demonstrated that the addition of Fe increases the solubility of $MgSiO_3$ in Ca-rich cubic perovskite coexisting with bridgmanite, with a (Mg,Fe) solubility of nearly 0.34 cations per formula unit at 78 GPa. It has also been shown that Al_2O_3 partitions preferentially into bridgmanite coexisting with davemaoite (Ricolleau et al., 2008). Given the shape of the davemaoite grain and thickness of the sample, however, it is also possible that the measurement encompasses small amounts of other phases as well. As noted earlier, the measured lattice parameters for the davemaoite in this study are larger than expected. We conclude that the overestimation could be a result of nonhydrostatic stress conditions.

While we were unable to make EDS measurements on the bridgmanite in this study because of its small grain size, we were able to put some constraints on its composition. In XRD measurements on a recovered thin section, we detected the $LiNbO_3$ structure, which corresponds to decompressed bridgmanite. Dorfman et al. (2012) also decompressed an Alm54 sample directly from 84 GPa to ambient pressure, and some of its diffraction peaks are consistent with a $LiNbO_3$-type rhombohedral structure as previously reported for pyrope-almandine compositions (Funamori et al., 1997; Kesson et al., 1995). Alm100 synthesized at 90 GPa and decompressed to 5 GPa retained the orthorhombic structure but had $LiNbO_3$ peaks at ambient pressure. Z. Liu et al. (2020) determined that bridgmanite with more than 33 mol% $FeAlO_3$ transforms into the $LiNbO_3$-type phase upon decompression. We identified several diffraction peaks corresponding to the $LiNbO_3$ structure in the XRD patterns collected on the recovered K11 thin section (Figure S2 in Supporting Information S1), indicating that the $FeAlO_3$ content of the high pressure bridgmanite was greater than 33 mol%. The $LiNbO_3$ in our sample has lattice parameters of $a = 4.863$ Å and $c = 12.749$ Å, resulting in a molar volume of 26.207 cm³/mol. Using the linear fit for $LiNbO_3$ volumes along the $MgSiO_3$-$FeAlO_3$ join from Z. Liu et al. (2020), we estimate that the bridgmanite in this sample contains 32 mol% $FeAlO_3$, which is within 1% of the 33 mol% bound referenced above. This estimate falls within the range where Z. Liu et al. (2020) saw bridgmanite at 0 GPa rather than $LiNbO_3$, but it is likely that the $LiNbO_3$ in our study has additional components besides just $FeAlO_3$, such as $AlAlO_3$, which would act to decrease the volume. PerpleX calculations suggest that our garnet composition should create a bridgmanite with majority $MgSiO_3$ and $FeAlO_3$ components (Figure 7b). At the conditions of K11 (52 GPa) in the subsolidus region, one expects ~41 mol% $MgSiO_3$, 39 mol% $FeAlO_3$, 14 mol% $AlAlO_3$, and 6 mol% $FeSiO_3$.

Previous studies have documented the effects of Fe^{3+} and Al substitutions into the bridgmanite structure and shown that the $FeAlO_3$ component increases the molar volume of bridgmanite (Huang et al., 2021; Z. Liu et al., 2020; Vanpeteghem et al., 2006). To investigate this in the present study, bridgmanite lattice parameters and volumes (Figure 8) were obtained as a function of pressure for samples where more than three bridgmanite peaks could be distinctively identified upon quenching after laser heating. Unit cell volumes were calculated from bridgmanite lattice parameters and fitted to a second-order Birch-Murnaghan equation of state. Fitted parameters are listed in Table 3. These are compared to the results of Dorfman et al. (2012), which include Alm100 and Alm54 ($Alm_{54}Pyr_{43}Grs_3Sps_1$), as well as Alm0 (pure pyrope, which forms $(Mg_{0.75}Al_{0.25})$ $(Si_{0.75}Al_{0.25})O_3$ bridgmanite) from Walter et al. (2004), $MgSiO_3$ from Lundin et al. (2008), $(Mg_{0.64}Fe_{0.36})$ $(Si_{0.64}Al_{0.36})O_3$ from Boffa Ballaran et al. (2012), and $(Mg_{0.5}Fe_{0.5})$ $(Si_{0.5}Al_{0.5})O3$ from Z. Liu et al. (2020). While the almandine component of our sample is most similar to Alm54, slight differences in the proportions of components of our sample $(Alm_{52}Py_{34}Gr_{11}Sp_2And_1)$ versus the Alm54 sample may cause the higher lattice parameter values seen in our samples, which overlap with Alm100 (Dorfman et al., 2012). Differences in lattice parameters can be attributed to inclusion of the $AlAlO_3$ component as well as small amounts of Ca into the bridgmanite structure (Huang et al., 2021; Ko et al., 2022). Because our samples were not loaded in a pressure medium (other than five samples with Ir foil) and were not mixed with gold or platinum (like the samples of Dorfman et al. (2012) and Walter et al. (2004)), this may also affect the stress state, pressure reading, and bridgmanite composition.

For further context, we also calculated phase proportions and bridgmanite component proportions for pure almandine using our modified input files as well as the original Stixrude and Lithgow-Bertelloni (2022) data (Figure 9). We demonstrate that the inclusion of hcp and fcc iron in addition to the $FeAlO_3$ endmember of bridgmanite results in a notably different P-T phase space and bridgmanite composition. At 2100 K, the $FeAlO_3$ component is predicted to reach a maximum of 18 mol% at 43 GPa. Dorfman et al. (2020) found that an almandine with an initial $Fe^{3+}/\Sigma Fe$ of 18% created a bridgmanite with 12% $Fe^{3+}/\Sigma Fe$ at 99 GPa, which, if correct, indicates that the Fe was somehow reduced. No accompanying phases were detected in the XRD patterns. The observation of a single bridgmanite phase does not align with our PerpleX predictions, but the quantity of Fe^{3+} roughly aligns with our prediction of $FeAlO_3$ content. Huang et al. (2021) suggest that an increasing amount of the $FeAlO_3$
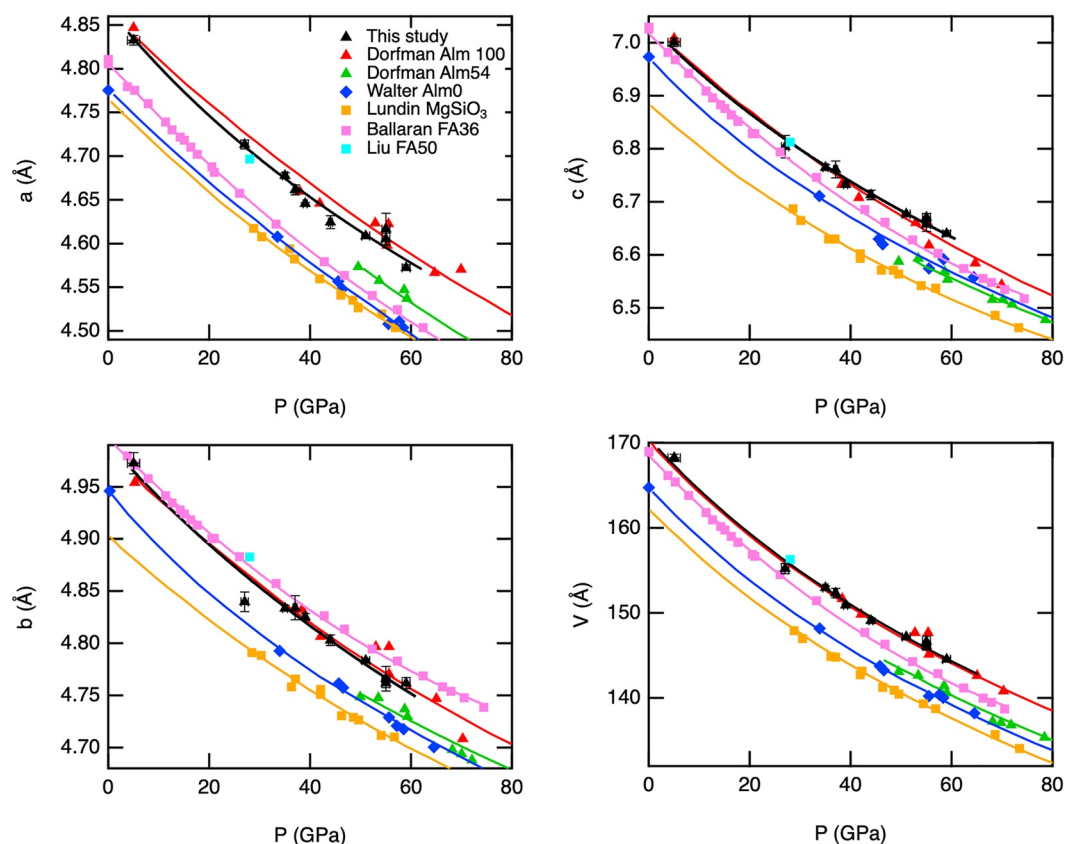
Figure 8. Lattice parameters of bridgmanite from this study (black triangles) compared with Dorfman et al. (2012) almandine100 (red triangles) and almandine54 (green triangles), Walter et al. (2004) almandine0 (blue diamonds), Lundin et al. (2008) $MgSiO_3$ (orange squares), Ballaran et al. (2012) (pink squares), and Z. Liu et al. (2020) (cyan squares).

component in bridgmanite should result in the c lattice parameter increasing the most and the b lattice parameter increasing more than the a lattice parameter, which is reflected in our results as well as those of other studies plotted in Figure 7, including Alm100, confirming the PerpleX results.

5. Conclusions

Fe metal was positively identified in an $Alm_{52}Py_{34}Gr_{11}Sp_2And_1$ composition from 39 to 64 GPa using SEM analyses, and from 28 GPa upward, bridgmanite is detected with XRD, which suggests that Fe metal was formed at these conditions as well through a disproportionation reaction. Thus, at lower mantle conditions (28–65 GPa), Fe metal is a stable part of the phase assemblage, having been produced by disproportionation of Fe, as has been observed in other mafic compositions. The lower mantle will not have the same quantity of disproportionated metallic Fe as was observed in this study, but the results nonetheless provide compelling experimental evidence across a significant range of lower mantle-relevant conditions that the incorporation of an $FeAlO_3$ component into bridgmanite will promote the disproportionation reaction. The PerpleX results also suggest that the amount of the $FeAlO_3$ component in bridgmanite decreases at higher pressures, which corresponds to a decrease in the amount of disproportionated metallic Fe with increasing pressure. The $FeAlO_3$ component may affect the elastic properties of bridgmanite, and the metallic Fe can alloy with siderophile and volatile elements in the lower mantle, affecting their distribution.

The phase assemblage in this study also consists of bridgmanite, stishovite, corundum, and davemaoite, as determined by X-ray diffraction, and is consistent with prior work (Dorfman et al., 2012; Kesson et al., 1995).

Table 3
Third-Order Birch-Murnaghan Fit Parameters for Bridgmanite

Composition	V_0 (Å)	K_0 (GPa)	K'_0
$Alm_{52}Pyr_{34}Grs_{11}Sps_2And_1$	170.5	257.6	4[a]
$Alm_{54}Pyr_{43}Grs_3Sps_1$[b]	165.6	261	4[a]
Alm100[b]	170.6	252	4[a]
Alm0[c]	164.85	253.4	4[a]

[a]Parameter fixed during the fit. [b]Dorfman et al. (2012). [c]Walter et al. (2004).
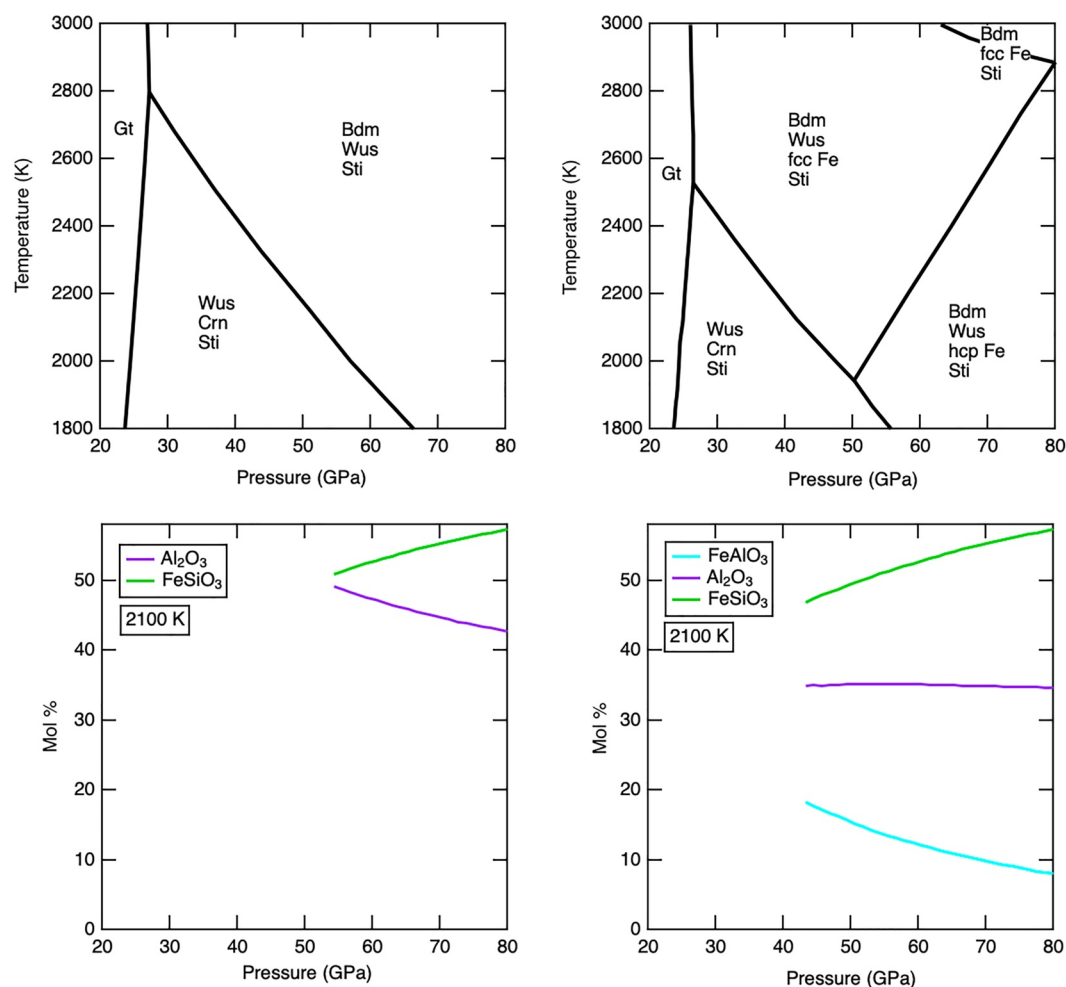
Figure 9. PerpleX phase assemblage and bridgmanite composition predictions for pure almandine with the original Stixrude and Lithgow-Bertelloni (2022) input files (left panels) and our modified files (right panels).

However, because of the low abundance of Fe metal and small grain size, XRD was not sufficient to detect the disproportionation reaction, and examination of the recovered product by FIB/SEM was required. The bridgmanite was found to decompress to the $LiNbO_3$-type structure, indicating a high $FeAlO_3$ content, which was confirmed with PerpleX predictions.

Data Availability Statement

Thermodynamic calculations were performed using PerpleX (version 6.8.9), an open-source software (Connolly, 2009). Bridgmanite lattice parameter values and volumes are archived on Zenodo and can be accessed at Swadba et al. (2023).

References

Akahama, Y., & Kawamura, H. (2004). High-pressure Raman spectroscopy of diamond anvils to 250 GPa: Method for pressure determination in the multimegabar pressure range. *Journal of Applied Physics*, *96*(7), 3748–3751. https://doi.org/10.1063/1.1778482

Akaogi, M., Ohmura, N., & Suzuki, T. (1998). High-pressure dissociation of $Fe_3Al_2Si_3O_{12}$ garnet: Phase boundary determined by phase equilibrium experiments and calorimetry. *Physics of the Earth and Planetary Interiors*, *106*(1–2), 103–113. https://doi.org/10.1016/S0031-9201(97)00084-8

Armstrong, L. S., Walter, M. J., Tuff, J. R., Lord, O. T., Lennie, A. R., Kleppe, A. K., & Clark, S. M. (2012). Perovskite phase relations in the system $CaO–MgO–TiO_2–SiO_2$ and implications for deep mantle lithologies. *Journal of Petrology*, *53*(3), 611–635. https://doi.org/10.1093/petrology/egr073

Ballaran, T. B., Kurnosov, A., Glazyrin, K., Frost, D. J., Merlini, M., Hanfland, M., & Caracas, R. (2012). Effect of chemistry on the compressibility of silicate perovskite in the lower mantle. *Earth and Planetary Science Letters*, *333*(334), 181–190. https://doi.org/10.1016/j.epsl.2012.03.029

Campbell, A. J. (2008). Measurement of temperature distributions across laser heated samples by multispectral imaging radiometry. *Review of Scientific Instruments*, *79*(1), 015108. https://doi.org/10.1063/1.2827513

Cerenius, Y., & Dubrovinsky, L. (2000). Compressibility measurements on iridium. *Journal of Alloys and Compounds*, *306*(1–2), 26–29. https://doi.org/10.1016/S0925-8388(00)00767-2

Chidester, B. A., Rahman, Z., Righter, K., & Campbell, A. J. (2017). Metal-silicate partitioning of U: Implications for the heat budget of the core and evidence for reduced U in the mantle. *Geochimica et Cosmochimica Acta*, *199*, 1–12. https://doi.org/10.1016/j.gca.2016.11.035

Connolly, J. A. D. (2005). Computation of phase equilibria by linear programming: A tool for geodynamic modeling and its application to subduction zone decarbonation. *Earth and Planetary Science Letters*, *236*(1–2), 524–541. https://doi.org/10.1016/j.epsl.2005.04.033

Connolly, J. A. D. (2009). The geodynamic equation of state: What and how [Software]. Geochemistry, Geophysics, Geosystems, *10*(10). https://doi.org/10.1029/2009GC002540

Conrad, P. G., Shen, G., Mao, H. K., Fei, Y., & Hemley, R. J. (1996). Stability of garnets in the system $MgSiO_3$–$FeSiO_3$–Al_2O_3 at high pressure. In *US–Japan seminar high pressure-temperature research: Properties of Earth and planetary materials* (Vol. 73).

Dorfman, S. M., Potapkin, V., Lv, M., Greenberg, E., Kupenko, I., Chumakov, A. I., et al. (2020). Effects of composition and pressure on electronic states of iron in bridgmanite. *American Mineralogist*, *105*(7), 1030–1039. https://doi.org/10.2138/am-2020-7309

Dorfman, S. M., Shieh, S. R., Meng, Y., Prakapenka, V. B., & Duffy, T. S. (2012). Synthesis and equation of state of perovskites in the (Mg, Fe)$_3$Al$_2$Si$_3$O$_{12}$ system to 177GPa. *Earth and Planetary Science Letters*, *357–358*, 194–202. https://doi.org/10.1016/j.epsl.2012.09.024

Fischer, R. A., Nakajima, Y., Campbell, A. J., Frost, D. J., Harries, D., Langenhorst, F., et al. (2015). High pressure metal-silicate partitioning of Ni, Co, V, Cr, Si, and O. *Geochimica et Cosmochimica Acta*, *167*, 177–194. https://doi.org/10.1016/j.gca.2015.06.026

Frost, D. J., & Langenhorst, F. (2002). The effect of Al_2O_3 on Fe-Mg partitioning between magnesiowustite and magnesian silicate perovskite. *Earth and Planetary Science Letters*, *199*(1–2), 227–241. https://doi.org/10.1016/S0012-821X(02)00558-7

Frost, D. J., Liebske, C., Langenhorst, F., McCammon, C. A., Tronnes, R. G., & Rubie, D. C. (2004). Experimental evidence for the existence of iron-rich metal in the Earth's lower mantle. *Nature*, *428*(6981), 409–412. https://doi.org/10.1029/200/JC000964

Fujino, K., Sasaki, Y., Komori, T., Ogawa, H., Miyajima, N., Sata, N., & Yagi, T. (2004). Approach to the mineralogy of the lower mantle by a combined method of a laser-heated diamond cell experiment and analytical electron microscopy. *Physics of the Earth and Planetary Interiors*, *143*(1–2), 215–221. https://doi.org/10.1016/j.pepi.2003.11.013

Funamori, N., Yagi, T., Miyajima, N., & Fujino, K. (1997). Transformation in garnet from orthorhombic perovskite to $LiNbO_3$ phase on release of pressure. *American Association for the Advancement of Science*, *275*(5299), 513–515. https://doi.org/10.1126/science.275.5299.513

Heinz, D. L., & Jeanloz, R. (1987). Temperature measurements in the laser-heated diamond cell. In M. H. Manghnani & Y. Syono (Eds.), *High-pressure research in mineral physics: A volume in honor of syun-iti akimoto*. https://doi.org/10.1029/GM039p0113

Huang, R., Boffa Ballaran, T., McCammon, C. A., Miyajima, N., & Frost, D. J. (2021). The effect of Fe-Al substitution on the crystal structure of $MgSiO_3$ bridgmanite. *Journal of Geophysical Research: Solid Earth*, *126*(9), e2021JB021936. https://doi.org/10.1029/2021JB021936

Irifune, T., Koizumi, T., & Ando, J. I. (1996). An experimental study of the garnet-perovskite transformation in the system $MgSiO_3$-$Mg_3Al_2Si_3O_{12}$. *Physics of the Earth and Planetary Interiors*, *96*(2–3 SPEC. ISS.), 147–157. https://doi.org/10.1016/0031-9201(96)03147-0

Kesson, S. E., Fitz Gerald, J. D., Shelley, J. M. G., & Withers, R. L. (1995). Phase relations, structure and crystal chemistry of some aluminous silicate perovskites. *Earth and Planetary Science Letters*, *134*(1–2), 187–201. https://doi.org/10.1016/0012-821X(95)00112-P

Knittle, E., & Jeanloz, R. (1987). Synthesis and equation of state of (Mg,Fe)SiO_3 perovskite to over 100 gigapascals. *Science*, *235*(4789), 668–670. https://doi.org/10.1126/science.235.4789.668

Ko, B., Greenberg, E., Prakapenka, V., Alp, E. E., Bi, W., Meng, Y., et al. (2022). Calcium dissolution in bridgmanite in the Earth's deep mantle. *Nature*, *611*(7934), 88–92. https://doi.org/10.1038/s41586-022-05237-4

Lauterbach, S., McCammon, C. A., Van Aken, P., Langenhorst, F., & Seifert, F. (2000). Mossbauer and ELNES spectroscopy of (Mg,Fe)(Si,Al)O_3 perovskite: A highly oxidised component of the lower mantle. *Contributions to Mineralogy and Petrology*, *138*(1), 17–26. https://doi.org/10.1007/PL00007658

Liu, L. G. (1976). Orthorhombic perovskite phases observed in olivine, pyroxene and garnet at high pressures and temperatures. *Physics of the Earth and Planetary Interiors*, *11*(4), 289–298. https://doi.org/10.1016/0031-9201(76)90016-9

Liu, Z., McCammon, C., Wang, B., Dubrovinsky, L., Ishii, T., Bondar, D., et al. (2020). Stability and solubility of the $FeAlO_3$ component in bridgmanite at uppermost lower mantle conditions. *Journal of Geophysical Research: Solid Earth*, *125*(2), e2019JB018447. https://doi.org/10.1029/2019JB018447

Liu, Z., Nishi, M., Ishii, T., Fei, H., Miyajima, N., Ballaran, T. B., et al. (2017). Phase relations in the system $MgSiO_3$-Al_2O_3 up to 2300 K at lower mantle pressures. *Journal of Geophysical Research: Solid Earth*, *122*(10), 7775–7788. https://doi.org/10.1002/2017JB014579

Lundin, S., Catalli, K., Santillán, J., Shim, S. H., Prakapenka, V. B., Kunz, M., & Meng, Y. (2008). Effect of Fe on the equation of state of mantle silicate perovskite over 1 Mbar. *Physics of the Earth and Planetary Interiors*, *168*(1–2), 97–102. https://doi.org/10.1016/j.pepi.2008.05.002

McCammon, C. (1997). Perovskite as a possible sink for ferric iron in the lower mantle. *Nature*, *387*(6634), 694–696. https://doi.org/10.1038/42685

O'Neill, B., & Jeanloz, R. (1990). Experimental petrology of the lower mantle: A natural peridotite taken to 54 GPa. *Geophysical Research Letters*, *17*(10), 1477–1480. https://doi.org/10.1029/GL017i010p01477

O'Neill, B., & Jeanloz, R. (1994). $MgSiO_3$-$FeSiO_3$-Al_2O_3 in the Earth's lower mantle: Perovskite and garnet at 1200 km depth. *Journal of Geophysical Research*, *99*(B10), 19901–19915. https://doi.org/10.1029/94JB01752

Prakapenka, V. B., Kubo, A., Kuznetsov, A., Laskin, A., Shkurikhin, O., Dera, P., et al. (2008). Advanced flat top laser heating system for high pressure research at GSECARS: Application to the melting behavior of germanium. *High Pressure Research*, *28*(3), 225–235. https://doi.org/10.1080/08957950802050718

Prescher, C., & Prakapenka, V. B. (2015). DIOPTAS: A program for reduction of two-dimensional X-ray diffraction data and data exploration. *High Pressure Research*, *35*(3), 223–230. https://doi.org/10.1080/08957959.2015.1059835

Richmond, N. C., & Brodholt, J. P. (1998). Calculated role of aluminum in the incorporation of ferric iron into magnesium silicate perovskite. *American Mineralogist*, *83*(9–10), 947–951. https://doi.org/10.2138/am-1998-9-1003

Ricolleau, A., Fiquet, G., Addad, A., Menguy, N., Vanni, C., Perrillat, J. P., et al. (2008). Analytical transmission electron microscopy study of a natural MORB sample assemblage transformed at high pressure and high temperature. *American Mineralogist*, *93*(1), 144–153. https://doi.org/10.2138/am.2008.2532

Shim, S. H., Duffy, T. S., & Shen, G. (2000). The equation of state of $CaSiO_3$ perovskite to 108 GPa at 300 K. *Physics of the Earth and Planetary Interiors*, *120*(4), 327–338. https://doi.org/10.1016/S0031-9201(00)00154-0

Shim, S. H., Grocholski, B., Ye, Y., Alp, E. E., Xu, S., Morgan, D., et al. (2017). Stability of ferrous-iron-rich bridgmanite under reducing midmantle conditions. *Proceedings of the National Academy of Sciences of the United States of America*, *114*(25), 6468–6473. https://doi.org/10.1073/pnas.1614036114

Stixrude, L., & Lithgow-Bertelloni, C. (2022). Thermal expansivity, heat capacity and bulk modulus of the mantle. *Geophysical Journal International*, *228*(2), 1119–1149. https://doi.org/10.1093/gji/ggab394

Swadba, K., Davis, A., Zurkowski, C., Chariton, S., Prakapenka, V., & Campbell, A. (2023). Dataset for "Disproportionation of iron in almandine-pyrope garnet from 25 to 65 GPa" [Dataset]. Zenodo. https://doi.org/10.5281/zenodo.8015609

Tsujino, N., Girard, J., Bi, W., Alp, E. E., & Karato, S. (2023). Formation of metallic Fe in bridgmanite under shallow lower mantle conditions. *Physics of the Earth and Planetary Interiors*, *337*(June 2022), 107010. https://doi.org/10.1016/j.pepi.2023.107010

Vanpeteghem, C. B., Angel, R. J., Ross, N. L., Jacobsen, S. D., Dobson, D. P., Litasov, K. D., & Ohtani, E. (2006). Al, Fe substitution in the MgSiO$_3$ perovskite structure: A single-crystal X-ray diffraction study. *Physics of the Earth and Planetary Interiors*, *155*(1–2), 96–103. https://doi.org/10.1016/j.pepi.2005.10.003

Walter, M. J., Kubo, A., Yoshino, T., Brodholt, J., Koga, K. T., & Ohishi, Y. (2004). Phase relations and equation-of-state of aluminous Mg-silicate perovskite and implications for Earth's lower mantle. *Earth and Planetary Science Letters*, *222*(2), 501–516. https://doi.org/10.1016/j.epsl.2004.03.014

References From the Supporting Information

Dewaele, A. S., Loubeyre, P., Occelli, F., Mezouar, M., Dorogokupets, P. I., & Torrent, M. (2006). Quasihydrostatic equation of state of iron above 2 Mbar. https://doi.org/10.1103/PhysRevLett.97.215504

Holland, T. J. B., & Powell, R. (2011). An improved and extended internally consistent thermodynamic dataset for phases of petrological interest, involving a new equation of state for solids. *Journal of Metamorphic Geology*, *29*(3), 333–383. https://doi.org/10.1111/j.1525-1314.2010.00923.x

Myhill, R. (2018). The elastic solid solution model for minerals at high pressures and temperatures. *Contributions to Mineralogy and Petrology*, *172*(2), 12. https://doi.org/10.1007/s00410-017-1436-z

Tsujino, N., Nishihara, Y., Nakajima, Y., Takahashi, E., Funakoshi, K. I., & Higo, Y. (2013). Equation of state of γ-Fe: Reference density for planetary cores. *Earth and Planetary Science Letters*, *375*, 244–253. https://doi.org/10.1016/J.EPSL.2013.05.040